PAPER

Low-density HiPIMS favored ultrathick and compact chromium coatings on Zircaloy-4 alloys

Physica Scripta

PAPER

Low-density HiPIMS favored ultrathick and compact chromium coatings on Zircaloy-4 alloys

RECEIVED
15 June 2023

REVISED
23 July 2023

ACCEPTED FOR PUBLICATION
17 August 2023

PUBLISHED
4 September 2023

Guangxue Zhou[1,3], **Xiao Zuo**[1], **Rende Chen**[1], **Zhenyu Wang**[1,3], **Peiling Ke**[1,2] and **Aiying Wang**[1,2,3]

[1] Key Laboratory of Marine Materials and Related Technologies, Zhejiang Key Laboratory of Marine Materials and Protective Technologies, Ningbo Institute of Materials Technology and Engineering, Chinese Academy of Sciences, Ningbo, 315201, People's Republic of China

[2] Center of Materials Science and Optoelectronics Engineering, University of Chinese Academy of Sciences, Beijing, 100049, People's Republic of China

[3] Ningbo Institute of Industrial Technology, Ningbo, 315201, People's Republic of China

E-mail: aywang@nimte.ac.cn

Keywords: HiPIMS, Cr coatings, ATFs cladding

Abstract

Protective metallic coatings are receiving increasing attention to modify the anti-corrosion and oxidation resistance of zirconium-based fuel cladding tubes under harsh high-temperature steam/air oxidation conditions. In this work, ultrathick (~20 μm) and compact Cr coatings with (001) preferential orientation were deposited on Zircaloy-4 (Zry-4) alloy by high power impulse magnetron sputtering (HiPIMS) technique. The growth characteristics of the Cr coatings were investigated as a function of the discharge plasma species, including Cr^+, Cr^*, Ar^+, and Ar^*, which were controlled by the different discharge modes during HiPIMS process. The results showed that, when the discharge feature was changed from the 'low voltage direct current magnetron sputtering (DCMS)-like' mode into a 'low density HiPIMS' mode, a rapid increase of Cr^+ content in the substrate vicinity was obtained by time-integral optical emission spectra (OES), indicating a remarkably enhanced incident energy flux to the deposited Cr coating. The generalized temperature increment of the Cr coating growing surface calculated from the OES, was ~100 K and was mainly affected by the incidence of Cr^* atoms. A simplified collision model based on the non-penetrating ions/atoms assumption was also proposed to calculate the transferred energy from the incident energetic species and thus understand the predominant effect of HiPIMS Cr plasma on the achieved nanocrystalline Cr coating with ultra-thick and dense structure, which is still quite challenging for the DCMS deposition process.

1. Introduction

With the rapid development of the nuclear power system as a clean and sustainable energy source, Accident Tolerant Fuel (ATF) technology is of increasing importance to enhance the safety and competitiveness of commercial nuclear power plants under harsh high-temperature steam/air oxidation (Loss of Coolant Accident, LOCA) environments [1]. The damage durability is of particularly critical for zirconium-based alloys, which are commonly used as fuel cladding in light water reactors (LWRs) [2]. To date, one effective solution is to replace the bulk refractory zirconium-based alloys by the advanced ceramic and fibric composites such as SiC and C/C candidates, which exhibit the combined high performance of corrosion and oxidation resistance as well as mechanical properties. However, there is still a long way to go to realize these substitutions due to the complex structure of fuel cladding over large size within the nuclear reactors. An important alternative strategy is to employ surface coating technology to protect zirconium alloy substrates, where the coating candidates could be preferentially tailored to simultaneously provide excellent hardness, high chemical stability and thermal conductivity, and low neutron absorption cross section. Currently, protective coatings on zirconium cladding tubes can be categorized into three main types: metallic coatings (Fe-based alloys, Cr, Cr–Al, Ni–Cr, etc), non-metallic coatings (oxides, nitrides, carbides), and innovative MAX-phase coatings (Cr_2AlC, Ti_2AlN etc) [1–5]. Among these coatings, metallic Cr coating has been recognized as a promising protective candidate considering

its satisfactory performance under both normal and LOCA conditions. In particular, the relatively simple deposition process together with the low crystallization temperature of Cr increases its suitability for ATF protective coating [6].

Three main approaches have been developed for the deposition of Cr coatings on Zr substrates: plasma spraying [7, 8], laser beam scanning (LBS) [9], and physical vapor deposition (PVD) [1, 10–14]. A representative example of using plasma spraying to fabricate Cr coatings was demonstrated by Maier *et al* who deposited a ∼100 um thick Cr coating on a 300 mm-length zirconium alloy tube in a few minutes [8]. Moreover, these sprayed thick Cr coatings exhibited good oxidation resistance up to 1300 °C. Nevertheless, it was found that once the coating showed the porous structure and rough morphology, even the 80 μm-thick Cr coated zirconium alloy tubes (by LBS technique) could be easily damaged after steam oxidation at 1200 °C for 2000 s [9]. In comparison, dense Cr coatings of only 10 μm-thickness prepared by cathodic arc plating, one of the most commonly used PVD techniques, greatly suppressed the oxidation resistance at 1200 °C for 2000s [14]. Furthermore, previous research has proposed that for coatings deposited by PVD approach, there is a strong dependence of the high-temperature oxidation kinetics of Cr-coated Zircaloy-4 on the coating structures and grain sizes [15–17]. Similar results were also reviewed by Yang [18] and Liu [19], where the oxidation resistance related to the diffusion behavior could be modified to a large extent by an appropriate choice of compactness, thickness, porosity and integrity of Cr coatings during magnetron sputtering and arc ion plating processes.

It must be noted that, compared to arc ion plating with drawbacks caused by macroparticles, magnetron sputtering (MS) deposition is a relatively promising method to synthesize Cr coatings with both smooth surface and good uniformity over large size substrates. However, since the metal ionization flux and plasma density are quite weak in DCMS, the deposited Cr coatings always suffer from problems of coarse and loose columnar structures with many grain boundaries and pinhole defects, which provide direct penetration pathways for corrosive oxygen and hydroxyl ions and cause rapid durability degradation [20–23]. Increasing the deposition temperature could promote the diffusion of adatoms in parallel with the growth of the coating, reducing the boundary gaps between columnar grains and eliminating the growth defect of the coating [24–26], but the long-time deposition for thick coating would substantially deteriorate both the mechanical and chemical properties of zircaloy, due to the stimulated re-crystallization and rapid grain growth [27, 28]. An important point of view is that, if one keeps in mind of the structure zone diagram proposed by Anders [29], tailoring the energetic ion flux during the deposition processes offers the most interesting strategy to optimize the coating microstructure and related performance, which has also been also confirmed by Park and Stringer *et al* [14, 30].

HiPIMS, which combining the advantages of both sputtering and arc ion plating, is an innovative ionized PVD technique. The high plasma density ($10^{18}-10^{19}$ m^{-3}, 3 orders of magnitude higher than DCMS) and the highly ionized metal ion fraction (⩾30% compared to less than 10% for DCMS) allow for the fabrication of coatings with preferred orientation, nanocrystalline microstructure, mechanical and chemical properties etc [31–33]. However, a critical issue of HiPIMS is the low deposition rate compared to DCMS at the same average power. Anders *et al* [34, 35] studied this deposition-rate loss phenomenon and ascribed it to the less-than-linear increase of sputtering yield with energetic ions, high target back-attraction probability of the metal ions with typical values in the range 70%–90% during the pulse and sideway deposition regime. In this case, it is still a long-standing dilemma to achieve ultra-thick (⩾15 μm) and compact Cr coating by HiPIMS technique at low deposition temperature, which is of preliminary importance to satisfy the protective performance for zircaloy alloys serving in harsh air/steam oxidation conditions.

In this work, we prepared the ultra-thick and compact Cr coatings on zircaloy alloys using a home-made HiPIMS deposition system, where the low-density discharge mode was specially controlled to balance the advantage of high energetic ion flux and the disadvantage of low deposition rate for HiPIMS. The microstructural evolution of the Cr coatings was discussed in terms of the plasma characteristics, focusing on the incident energetic species and the discharged adatom lifetime estimated from optical emission spectra.

2. Experimental

2.1. Deposition of Cr coatings on Zry-4 alloys

Cr coatings were deposited on Zry-4 alloy substrates with a diameter of 10.0 mm and a thickness of 1.0 mm using a home-made hybrid HIPIMS system. The composition of the used Zry-4 alloys in wt% was 0.0094% Si, 0.12% Cr, 0.12% O, 0.21% Fe, 0.33% Fe + Cr, 1.28% Sn, and Zr as the balance. The pristine Zry-4 alloys were firstly polished with SiC abrasive paper to 2000 grit, and then were ultrasonically cleaned in acetone and ethanol solutions with 10 min for each step. After drying with compressed nitrogen, the Zry-4 substrates were placed in the sample fixture located in the deposition chamber. Figure 1 shows the schematic diagram of the employed deposition system. A rectangular Cr target with a purity of 99.99 wt% and with a dimension of 400 mm (length) × 100 mm (width) × 7 mm (thickness) was used as the metallic sputtering source, which was driven by

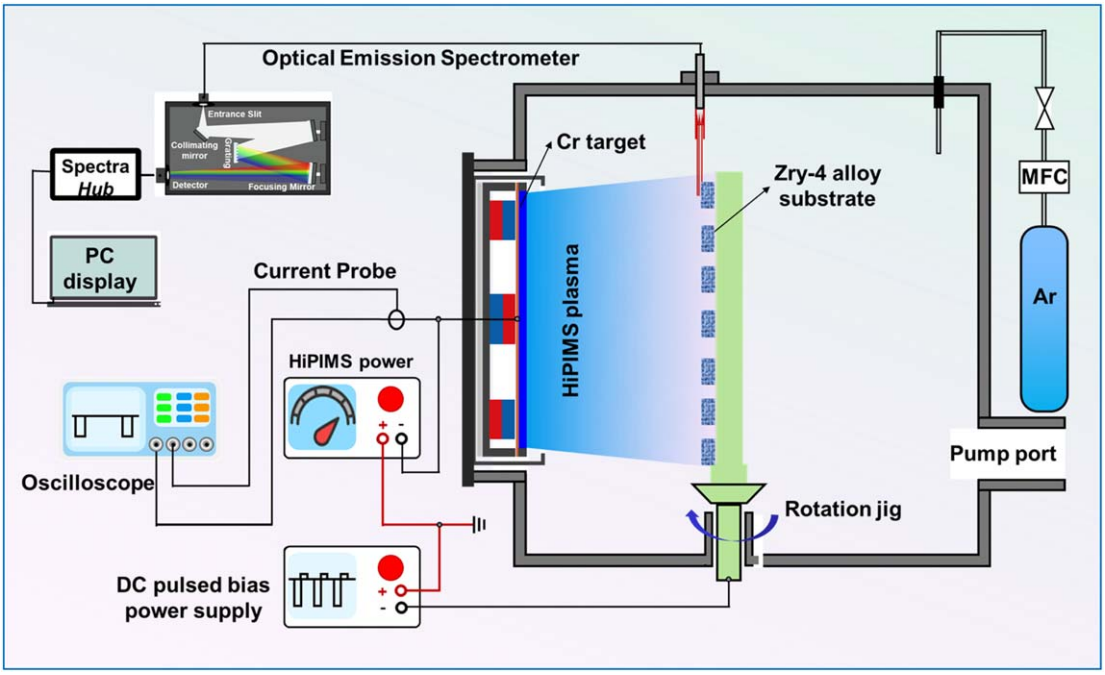

Figure 1. Schematic diagrams of used HiPIMS deposition system for Cr coating on Zry-4 alloys.

a HiPIMS power supply (SPIK 3000 A, MELEC GmbH). The perpendicular distance between the Zry-4 substrates and the Cr target was 120 mm. The chamber base pressure was 1.0×10^{-5} Torr. The deposition temperature was kept at 200 °C, as the Zry-4 alloys easily suffer from the phase transition and the deterioration of mechanical properties at temperatures above 500 °C. Subsequently, the Zry-4 alloys were pre-cleaned by Ar ions for 30 min at a working pressure of 15 mTorr, corresponding to the introduced 50 sccm Ar gas. This etching process was applied with a pulsed voltage of −600 V at a frequency of 350 kHz and a reversal time of 1.1 μs (Pinnacle® Plus+, AE). During deposition, the working pressure was controlled at 2.5 mTorr, and the Cr target was sputter-cleaned for 15 min. The Cr coating was then deposited under a −80 V dc pulsed bias. The substrates were rotated clockwise at 12 rpm throughout the whole deposition process.

2.2. Characterization and calculation of plasma discharge

The discharge voltage and current were monitored using a combined current transducer (LT58-S7, LEM) and a high voltage differential probe (UT-P32, UNI-T) [36]. Data were recorded with a 2-channel digital storage oscilloscope (TDS 1012C-SC, Tektronix). The time-averaged discharge current (I_a) was calculated using the following equation:

$$I_a = \frac{1}{T}\int_{t_0}^{T} i(t)dt \tag{1}$$

where, t_0 corresponds to the start time of a voltage pulse, T is the period of the pulse, $i(t)$ is the transient target current. The optical emission spectra (OES) signal of the HiPIMS-Cr plasma in the vicinity of the substrate was acquired via the optical fiber and analyzed by a spectrometer (Acton SP2500, Princeton Instruments), the installation details could be found in the previous publication [37].

The morphology of the deposited Cr coatings was characterized by a high-resolution field emission scanning electron microscope (Quanta FEG 250, FEI). Both the surface and cross-sectional views were presented for comparison. In addition, the detailed structural evolution of the coatings was measured by the electron backscatter diffraction (EBSD) module in the SEM system (Verios G4 UC, Thermo Scientific) with a resolution of 0.6 nm, in which the grain size, grain boundary, and crystallographic orientation of the coating could be elucidated.

The ratio of power-normalized HIPIMS and dc deposition rates with the variation of discharge voltage could be described as follows [38]:

$$\rho = K^{b-1} \tag{2}$$

Where K is the ratio of HiPIMS voltage to DCMS voltage under the same input power condition, while b is about 0.5. We see that the more the HIPIMS voltage is enhanced compared to the dc voltage, the greater is the reduction in the normalized HIPIMS deposition rate. The reason for this phenomenon is the severe

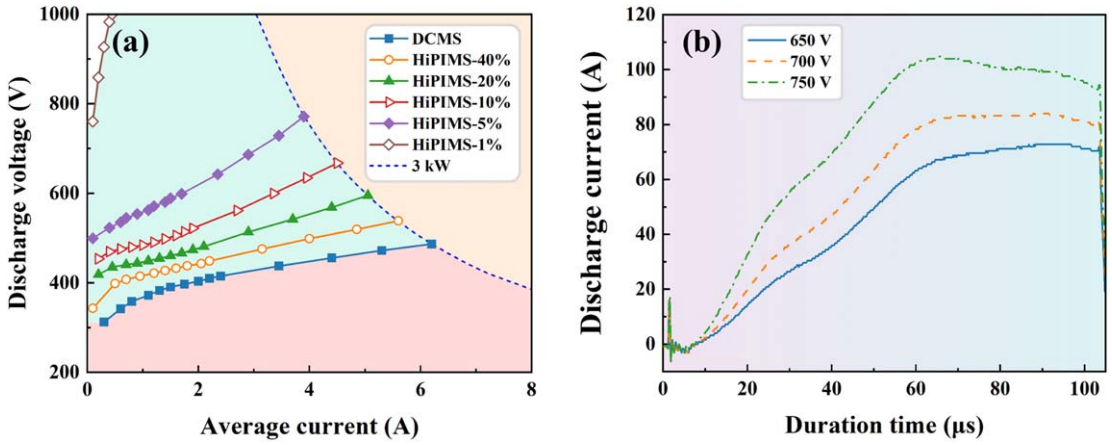

Figure 2. (a) voltage-current characteristics of DCMS-Cr and HiPIMS-Cr with various duty cycles, (b) representative discharge current waveforms of HiPIMS-Cr (5% duty cycle) at 650 V, 700 V, and 750 V.

self-sputtering along with the dense structure growth during the energetic incidence of highly ionized plasmas during HiPIMS. A promising approach to directly improve the deposition rate without sacrificing the other superior features of HiPIMS is to control the discharge voltage, which provides ability to manipulate the discharge mode from high-density to low-density, thus providing high performance coating with tailored properties.

3. Results

3.1. The voltage-current discharge characteristics

The voltage-current characteristics of HiPIMS-Cr discharge with the variations of duty cycle and discharge power were shown in figure 2. It could be seen that the voltage of DCMS-Cr at 3 kW was about 440 V (figure 2(a)). If the discharge voltage of HiPIMS-Cr was selected as 1000 V at the same power, the factor K would be 2.3 and the relative deposition rate would be about 0.66 as derived from equation (2). deduced from equation (2). This showed that the deposition rate in HiPIMS was reduced by about 34% compared to that of DCMS. Meanwhile, according to previous works [36, 37], when the pulse voltage was higher than 700 V, the HiPIMS-Cr discharge would change from the 'DCMS-like' mode to the 'low-density HiPIMS discharge' mode. In this case, a drastic improvement of the ionization degree of Cr atoms could be expected. To balance the ionization fraction and the deposition rate, the deposition of Cr layers was performed using with a frequency 500 Hz and a pulse width of 100 μs (duty cycles of 5%). Figure 2(b) shows the dependence of the discharge current waveforms on the discharge voltage of 650 V, 700 V, and 750 V, respectively. In general, the rise of the target current in HiPIMS has an apparent delay compared to the target voltage pulse, and it remains on at a nearly constant value (~10 μs) when the pulse voltage was between 650 and 750 V. Yushkov *et al* attribute this phenomenon to the time needed for ionization avalanches to grow and ionization cycles to complete [39]. The pulse current shapes for the 650 V and the 700 V discharges were similar, showing an almost linear increase and reaching plateau values of 72 A and 84 A, respectively. The plateau was stable throughout the rest of the pulse and was cut off at the end of the voltage pulse. The character of the current shape changed when the applied 'driving' voltage was increased to 750 V, it exhibited an initial peak of about 105. A shortly after the beginning of the HiPIMS pulse followed by a gradual decay phase characterized by a decrease in current until the end of the 100 μs pulse length, this process can be associated with the (i) electron impact ionization of the working gas as a result of the much higher plasma densities during the peak of the HiPIMS discharge current as compared to for example DCMS and (ii) Ar gas rarefaction (the depletion of sputter gas in the vicinity of the target) regime, where the heating is due to momentum transfer in collisions between the background gas and the increasing amount of sputter-ejected Cr atoms as well as reflected sputtering gas atoms, indicating the transition from the Ar gas-dominated discharge to the Cr self-sputtering mode [40].

3.2. The deposition of Cr coatings on Zry-4 alloys

HiPIMS deposition of thick (>15 μm) Cr coatings was quite time-consuming due to the reduced deposition rate. To quickly optimize the parameters, Cr coatings with a thin thickness of 4.1 ± 0.2 μm were first deposited on Zry-4 substrates at different discharge voltages (650 V, 700 V, and 750 V) to study the growth morphology of the resulting coatings. Figure 3 shows the corresponding in-plane and cross-sectional SEM images of the

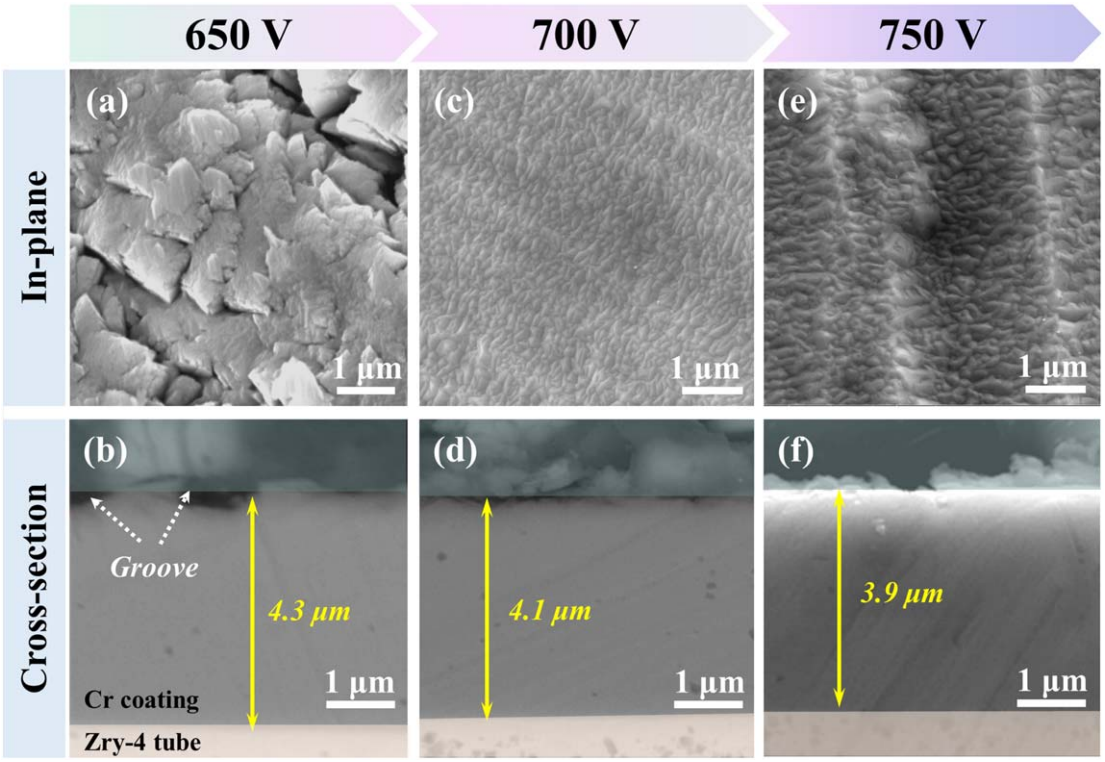

Figure 3. In-plane and cross-section SEM images of thin Cr coatings by HiPIMS process at 650 V, 700 V, and 750 V. The coating thickness was 4.1 ± 0.2 μm.

coatings. The surface of the Cr coating deposited at 650 V was rather rough and coarse, where the submicron grooves with pinholes acting as open defects were clearly visible and both the steam oxidation and corrosive resistance of Cr coatings at high temperature would be fatally reduced. Moreover, helium atoms and ions could easily penetrate along these defects to form short bubble microcracks in Zry-4 cladding tubes, causing unexpected disasters [41]. In comparison, the Cr coatings deposited at 700 V and 750 V showed both the smooth surfaces and compact microstructures, which could be correlated with the high current–voltage characteristics. Note that all the coating thicknesses were controlled at around 4.1 μm to avoid the thickness dependence on coating features.

Based on these results, further thick Cr coatings up to 20 μm were successfully fabricated on Zry-4 alloys under the pulse voltage of 700 V and 750 V, respectively. Figure 4 shows the corresponding surface topographies and cross-sectional morphologies. Both coatings were dense with no micro-cracks, and the interface between the Cr coatings and the Zry-4 substrates appeared to be defects-free, indicating a very good adhesion strength between the Cr–Zr interface. Furthermore, the Cr coating deposited at 750 V indicated a smoother surface after a long growth process than that at 700 V, which could be relevant to the higher peak power density (395 W cm^{-2} at 750 V > 290 W cm^{-2} at 700 V). In addition, the (001) preferred orientation with an average grain size of 90 nm in the compact structure was revealed by the EBSD measurement for the coating deposited at 750 V. In general, the higher power density could lead to the stronger electric field during the sputtering stage, optimizing the accelerated ion flux fraction and the diffusion ability of adatoms. As a result, the achieved ultrathick and compact Cr coating obtained enables the expected superior corrosion resistance in the steam environment up to 1200 °C [1].

For comparison, the surface topographies and cross-sectional morphologies of Cr coatings deposited on Zry-4 alloys by DCMS were further investigated and shown in figure 5. The deposition parameters, such as discharge power, working pressure, deposition temperature, substrate bias and deposition time were all kept at the same as those as those of the HiPIMS process with a pulse voltage of 750 V. Evidently, the DCMS-Cr coating had a greater thickness of 37.5 μm than that of HiPIMS-Cr with 19.8 μm, illustrating the higher deposition rate of DCMS. In addition, since the deposition was carried out at low temperature, significant grain boundary motion did not occur during coalescence or thickening, thus, Cr coating deposited at 200 ℃ by DCMS consisted of the typical large, tapered, and coarse columnar grains. This porous structure was unexpected, because it could provide a direct penetration path for oxygen/hydroxyl corrosive ions, causing the significant deterioration of the anti-oxidation behavior of coating. The HIPIMS coatings showed, on the other hand, denser structures.

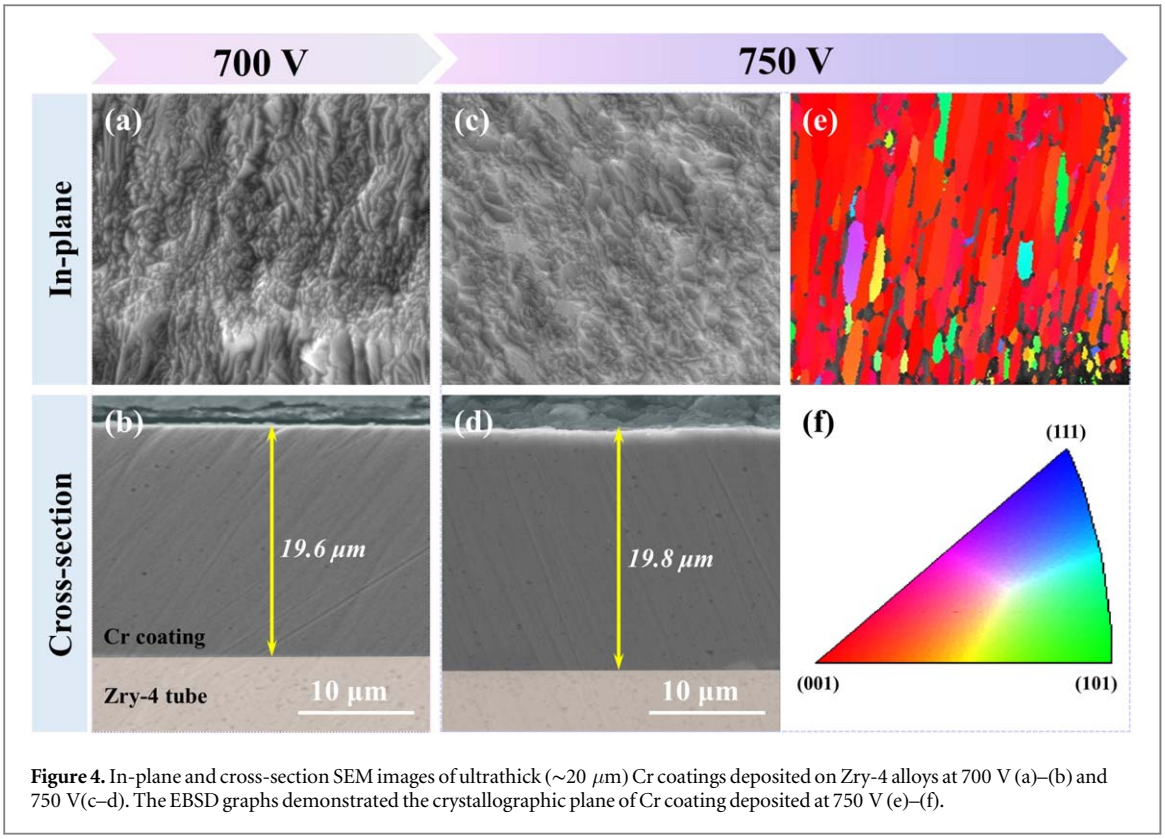

Figure 4. In-plane and cross-section SEM images of ultrathick (~20 μm) Cr coatings deposited on Zry-4 alloys at 700 V (a)–(b) and 750 V(c–d). The EBSD graphs demonstrated the crystallographic plane of Cr coating deposited at 750 V (e)–(f).

Concurrent bombardment of the growing surface by large fluxes of hyperthermal species can affect both surface and subsurface layers and thus trigger film nucleation and coalescence [42]. It has been shown that low-energy ion irradiation at ion energies $E^i_{kin} \leqslant 20$ eV enhances adatom surface diffusion leading to coatings with dense individual columns, but with open (underdense) column boundaries. Increasing the ion energy significantly above the bulk lattice displacement threshold, $\geqslant$20 eV depending on the material system (mass of the bombarding species and layer composition), will on the one hand reduce the voids between columns, but also, at high enough E^i_{kin}, significantly increase the defect density (incorporation of intragranular residual damage) so that renucleation occurs. As a result, considerably smaller grains form in the coating [43].

4. Discussion

4.1. Characterization of incident energetic species

Figure 6 shows the OES spectra and the deduced intensity of typical Cr and Ar spectral lines at different HiPIMS voltages in the vicinity of the substrate. As shown in figure 6(a), HiPIMS-Cr plasmas were mainly composed of typical lines of excited Cr atoms (Cr^*), Ar ions (Ar^+), excited Ar atoms (Ar^*), and a small amount of Cr ions (Cr^+). Under the assumption of direct electronic impact excitation from the ground state, uniform plasma emission and no re-absorption, the detected signal intensity corresponding to the $u \rightarrow l$ transition can be expressed as [44]

$$I_{ul} = [X^*_u] R_{ul} h\nu_{ul} A_{ul} d\Omega' \tag{3}$$

where, R_{ul} is the spectral response, ν_{ul} is the frequency of the emission light, A_{ul} is the transition probability, $[X^*_u]$ is the number density of Cr or Ar atoms in the 'u' state, $d\Omega'$ is the constant solid angle for each discharge condition. The optical emission spectral intensity can be used to indicate the ionization fraction of the HiPIMS-Cr plasma and the energization of the sputtered Cr atoms. In general, line intensities of Cr^+, Cr^*, Ar^+, and Ar^* showed an exponential growth with the increase of the discharge voltage, and the main impinging species on the growth surface were Cr^* and Ar^+. A surge in the intensity of the Cr^+ spectra line was observed when the pulse voltage was increased from 650 V to 700 V. This indicates a significantly enhanced proportion of metal ionization in the case of 700 V discharge. The detailed spectroscopic data of these four selected lines are presented in table 1. The influence of each incident energetic species on the coating microstructure will be analyzed in detail in the following subsections.

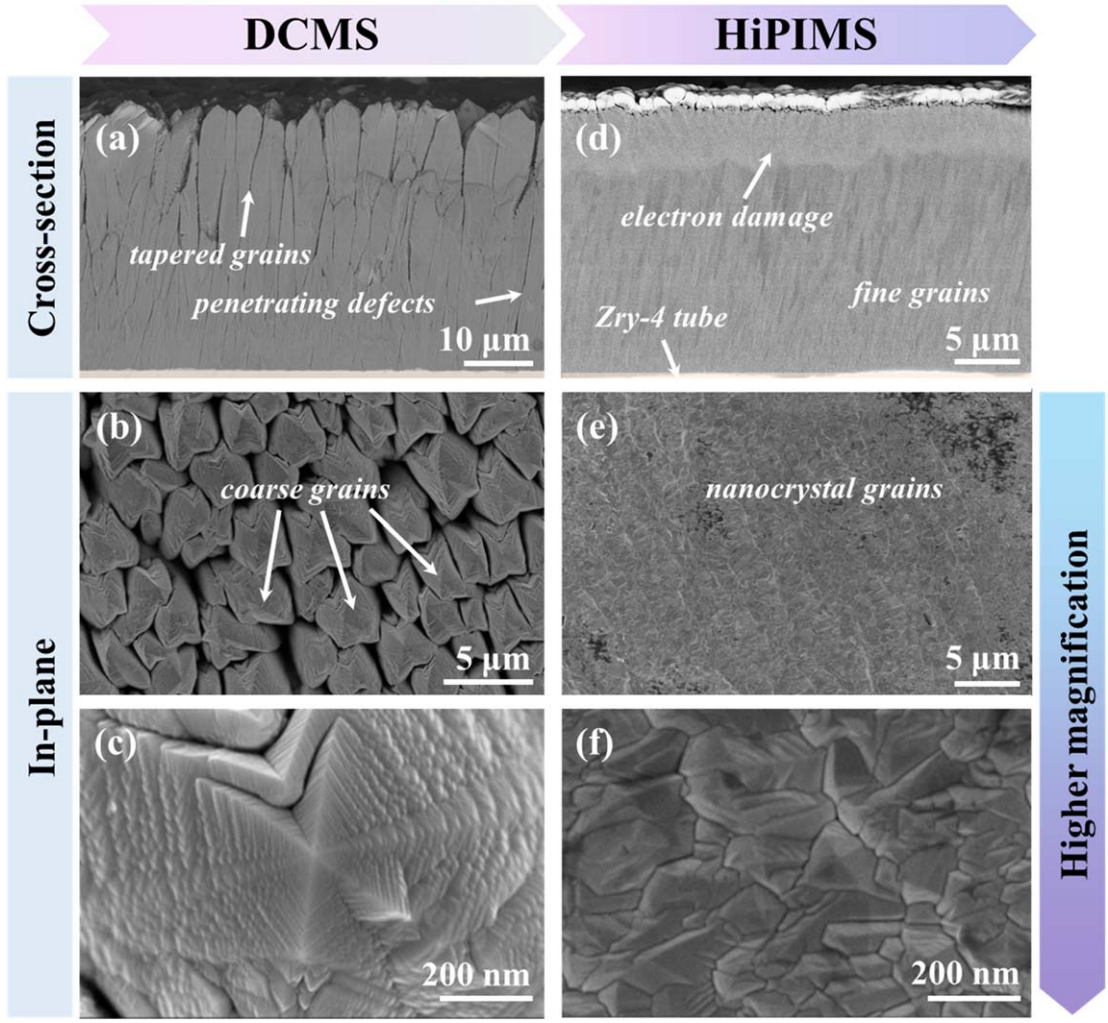

Figure 5. Cross-sectional morphologies and surface topographies of Cr coatings deposited on Zry-4 alloys by DCMS (a)–(c) and HiPIMS(d)–(f). The DCMS-Cr coating displays coarse columnar grains, while dense nanocrystalline structure is presented in the HiPIMS-Cr coating.

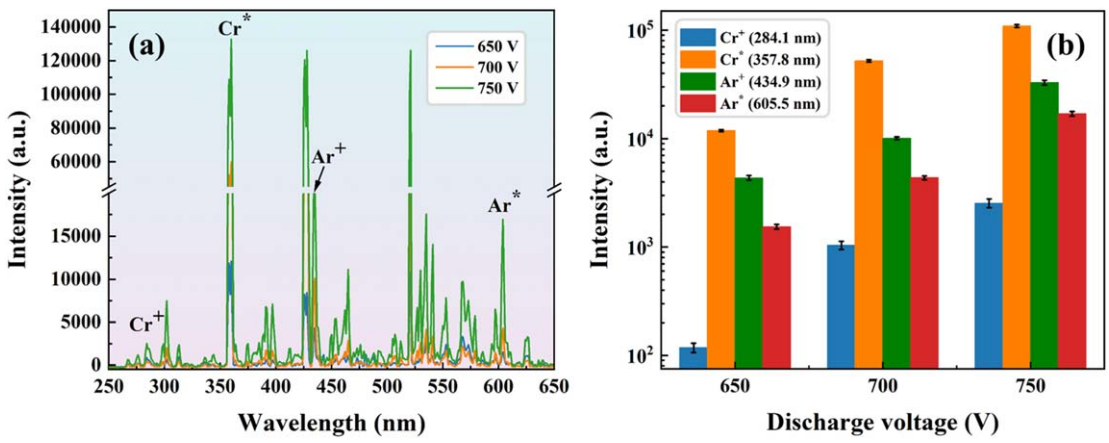

Figure 6. (a) OES spectra of HiPIMS-Cr plasmas in the substrate vicinity, (b) the increase of typical Cr and Ar spectral lines with the variation of discharge voltage.

4.2. Incidence of energetic species

Due to a significant reduction in the thermal electron flux to substrates reported for HiPIMS deposition processes, the increase of substrate temperature caused by electrons should be negligible [45, 46]. However, the

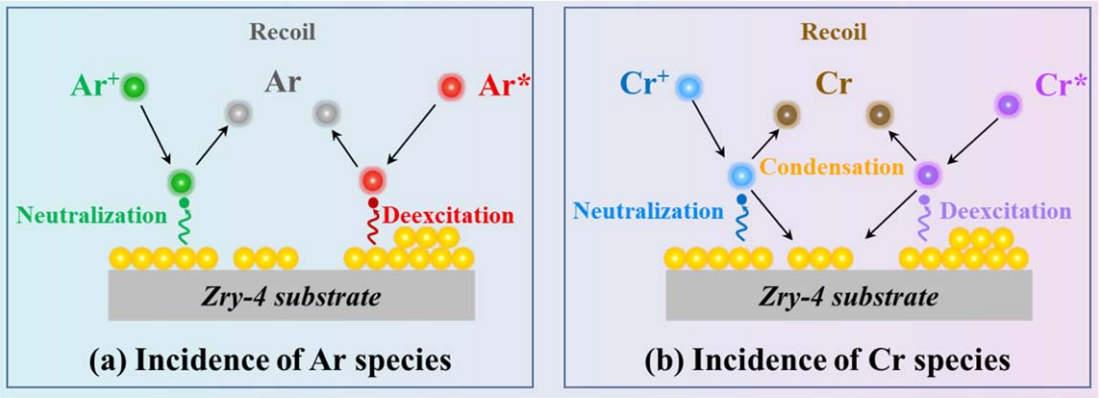

Figure 7. Schematic representation illustrating neutralization, deexcitation, condensation, and recoil processes during the incidence of energetic (a) Ar and (b) Cr species.

Table 1. The spectroscopic data of typical spectral lines. λ is the wavelength, E_u is the energy of the upper level, E_l is the energy of the lower level.

Species	λ (nm)	E_l (eV)	E_u (eV)	Low level	Transition
Cr^+	284	3.76	8.15	—	$Z\,^4I^\circ \rightarrow a\,^4H$
Cr^*	358	0.00	3.46	Ground	$Y\,^7P^\circ \rightarrow a\,^7S$
Ar^+	435	16.64	19.49	—	$3s^23p^44p \rightarrow 3s^23p^44s$
Ar^*	606	13.09	15.14	Radiative	$3s^23p^55d \rightarrow 3s^23p^54p$

temperature on the growing surface can be modified by the potential energy of arriving heavy species. The potential energy of incident Cr^+ includes the cohesive energy as well as the ionization energy reduced by the work function of the electron needed for the neutralization effect [29]. Deexcitation of Cr^* also contributes to the as discussed potential energy. Incident Ar^+ and Ar^* will also be neutralized and deexcited by electrons. But the absorption of Ar on the growth surface is negligible, the cohesive energy of Ar wouldn't contribute to the potential energy. Taking into account of the detachment of incident ions/atoms, we introduce the sticking probability (α) [47], neutralization (ρ_n), and deexcitation (ρ_d) coefficients of incident ions/atoms on the growth surface. A schematic representation of the processes during the incident of energetic species is shown in figure 7. The ground-state Ar atoms have no potential energy contribution, while the ground-state Cr atoms have only cohesive energy parts.

The potential energy (E^i_{pot}) produced by the incident species i can be expressed as

$$E^i_{pot} = \alpha^i E^i_c + \beta^i (E^i - \varphi^i) \tag{4}$$

where, E^i_c is the cohesive energy, E^i is the ionization or excitation energy, φ^i is the work function of the target materials. The potential energy flux weighted by the fraction of the species i arriving at the growth surface is

$$E_{pot} = \sum_i E^i_{pot} \cdot J^i \tag{5}$$

J^i is the incident species flux of species i. The characteristic temperature (T_{pot}) of a heated region affecting the rearrangement of N moved atoms by the potential energy is

$$T_{pot} = \frac{1}{k_B} \sum_i \frac{E^i_{pot} \cdot J^i}{N^i} \Big/ \sum_i J^i \tag{6}$$

k_B it the Boltzmann constant. We assume that the thermal spike is roughly hemispherical as shown in figure 8, the volume of the heated region (thermal spike) is proportional to $(E - E_B)$ [48, 49]. $E - E_B$ is the energy of the incoming species minus the energy required to overcome the potential barrier to arrive at the Cr coating growing surface, E_B is the surface binding energy of target materials. Once energetic species arrived in the surface, their remaining energy will be distributed among neighboring atoms. Thus, the number of moved atoms can be calculated by the following equations:

$$d^i_{spike} = 6a_0(E - E_B)^{1/3} = 6a_0(E^i_{pot})^{1/3} \tag{7}$$

$$V^i_H = 18\pi a_0^3 E^i_{pot} \tag{8}$$

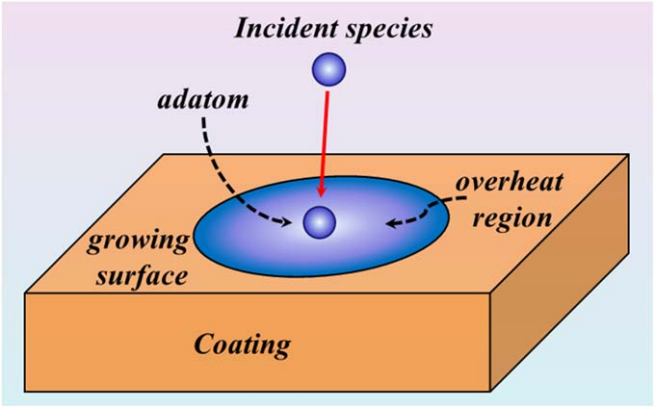

Figure 8. Conceptual model of the heat region (thermal spike) generated by incident energetic species. The incident species is shown in blue. The deep blue region surrounding it contains atoms which have gained enough energy from the impact to reconfigure their bonding.

$$N^i = \frac{V_H^i \cdot \rho_{Cr}}{51.99 \times 1.66 \times 10^{-27}} \tag{9}$$

where d_{spike}^i is the diameter of the heat region in nanometer, a_0 is the lattice parameter of bcc Cr material, ~0.291 nm. $\rho_{Cr} = 7.19\ \mathrm{g\,cm^{-3}}$ is the mass density of Cr in the solid state.

The kinetic energy of arriving ions consists of an initial component from the plasma (E_0) plus a change due to acceleration in the substrate sheath, $E_{kin} = E_0 + eU_{sheath}$, where e is the elementary charge, U_{sheath} is the voltage drop between the plasma and the substrate surface. The initial kinetic energy of sputtered species at low pressure can be approximately described by the Thompson distribution, which has a maximum at $E_B/2$ and a tail ~E^{-2}. Therefore, the kinetic energy of incident Cr^+ can be expressed as:

$$E_{kin}^{Cr^+} = \tilde{E}_{sput} + eV_{sheath} \tag{10}$$

The kinetic energy of Cr^* atoms is the Thompson distribution ($\tilde{E}_{sput}$). Ar^+ ions and Ar^* atoms arriving at the Cr coating growing surface also contribute to the potential energy with their ionization and excitation energies. Ar^+ can also cause momentum transfer when colliding with the adatoms and result in the loss of kinetic energy. After collisions with the growth surface, Ar^+ will be reflected back to the plasma in the form of neutral Ar atoms whose energy is less than ~10 eV [29]. Therefore, the initial kinetic energy of Ar^+ and Ar^* can be estimated to be 10 eV. The energy flux is weighted by the fraction of arriving species and normalized by the cohesive energy (E_c). The reduced kinetic energy factor can then be written as [29]

$$E^* = \sum_i \frac{E_{kin}^i}{E_c} \frac{m^i}{m_s} \cdot J^i / \sum_i J^i \tag{11}$$

m_s is the mass of atoms in the coating growing surface.

The cohesive energy and ionization energy of Cr atoms are ~5.33 eV $\mathrm{atom^{-1}}$ and 6.77 eV $\mathrm{atom^{-1}}$, respectively. In this study, only single-charged Cr ions (Cr^+) were considered because no multi-charged Cr ions (Cr^{n+}, $n > 1$) were detected in the OES spectra. The work function φ of Cr is about 4.1 eV[48]. Since the Zry-4 alloys were installed in front of the Cr target, the incident angle of the energetic species on the growing surface of the Cr coating could be determined by the velocity of the incident species and the self- rotation velocity of the substrates. As the incident velocity is much higher than the self-rotation speed, the off-normal angle (θ) of incidence is approximately as 0°. According to the work published by H Wu and A Anders [50], the sticking probability for metal ions/atoms on the growing surface was 1.0 under vertical incidence. Therefore, it is reasonable to assume that the sticking probability for Cr^+ ions and Cr^* atoms with a value of 1.0 in this study. The sticking probability of Ar^+ ions and Ar^* atoms on the metal surface varied with incident energy, angle, and lattice temperature. W. Lee *et al* calculated the sticking probability of argon in various metal films [51]. The sticking probability of argon in Cr film under 1.5 kV cathode drop and ballistic transport conditions has a value of 1×10^{-9}. It is known that the sticking probability of argon in metal films is positively correlated with the incident energy. Therefore, the sticking probability of argon in our study can be close to 0. When ions and excited atoms were attached on the Cr coating growing surface, they should be neutralized and deexcited. Here, the neutralization and deexcitation coefficient of Cr ions/atoms attached to the growing surface was 1.0. Overall, the neutralization and deexcitation coefficient for Ar ions/atoms of energy less than 100 eV during the inward journey is about one [52]. The ionization and excitation energies for Ar and Cr species can be found in

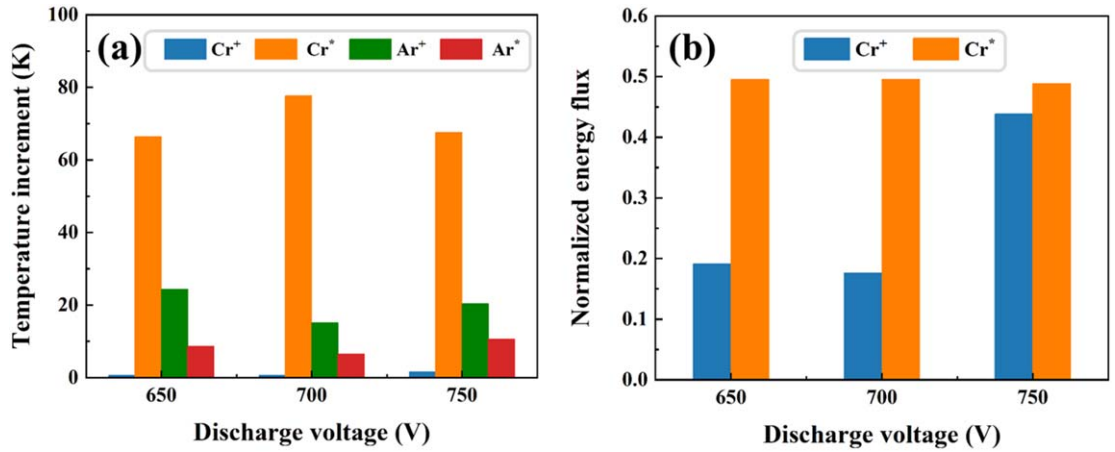

Figure 9. The temperature increment at growing surface (a) and the normalized energy flux (b) from the incident energetic species.

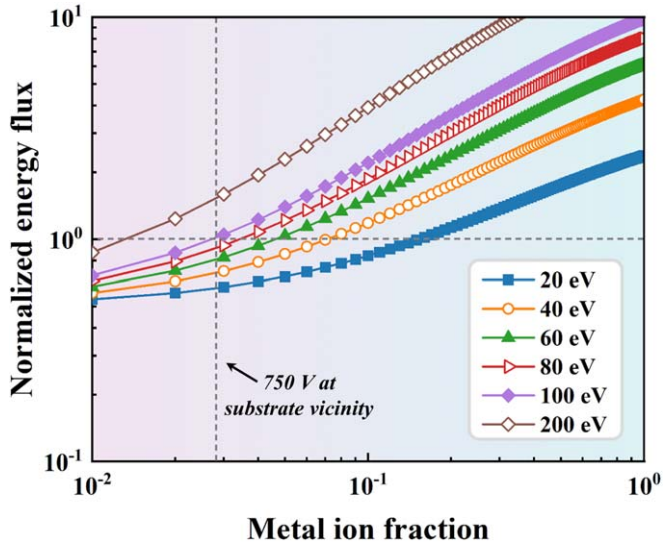

Figure 10. The variation of normalized energy flux with the metal ion flux fraction under different substrate bias conditions.

table 1. The averaged kinetic energy of sputtered Cr atoms was calculated from the Thompson distribution, which is around 2.67 eV.

Finally, the contribution of the energetic species to the generalized temperature and normalized energy flux was evaluated and shown in figure 9(a). HiPIMS-Cr deposition at 650 V, 700 V, and 750 V have almost the same contribution to the temperature increment. The growing surface temperature increased a same value of ~100 K during HiPIMS-Cr deposition for all three pulse voltage conditions. In contrast, the corresponding normalized energy flux for HiPIMS-Cr at 650 V, 700 V, and 750 V was significantly improved from 0.67, through 0.68, and finally to 0.93, respectively. As we can see from figure 9(a), the increase in surface temperature was mainly come from Cr^*, while Ar^+ also played an important role. Meanwhile, both Cr^+ and Cr^* contribute to the normalized energy flux. It has been demonstrated that the contribution from Cr^* atoms was kept almost constant for all the three pulse conditions, with $E_{kin}^{Cr^*} \approx 0.5$. However, when the discharge transferred from the 'DCMS-like mode' to the 'low-density HiPIMS mode' at 750 V, the contribution from Cr^+ was drastically increased from ~0.2 to 0.45. This result indicated the important role of incident metal ions under the control of a substrate bias. Furthermore, the relationship between the Cr ion flux fraction ratio (the content ratio of Cr^+ ions/Cr^* atoms) and the normalized energy flux was calculated and shown in figure 10. It is predicted that as the Cr^+ flux fraction is further improved, the normalized energy flux can be more effectively modified by the substrate bias.

4.3. Estimated adatom lifetime under the incident of energetic species

The energy transfer can be estimated by a simplified species collision model by assuming normal and non-penetrating incidence of the energetic species [53]. Assuming that the atoms (with the gross mass $M^i = N^i m_s$)

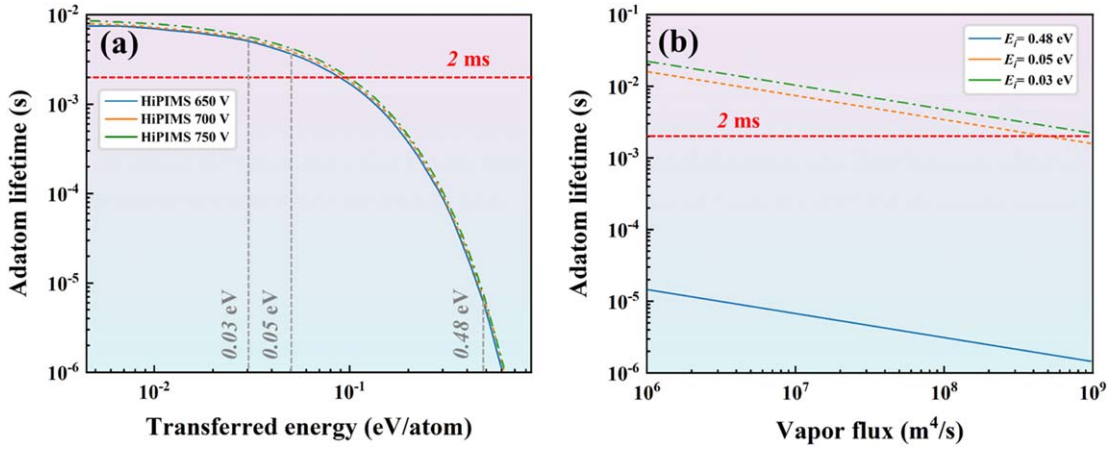

Figure 11. The variation of absorbed chromium atoms with the transferred energy per incident specie and vapor flux.

in the interaction zone (blue hemisphere in figure 8) are initially stationary, the energy transfer (ΔE) could be expressed as

$$\Delta E = \left(\frac{4m^i M^i}{(m^i + M^i)^2}\right) E^i_{tot} \tag{12}$$

The impacted adatom gains an averaged energy transferred from the incidence of each Cr^+, Cr^*, Ar^+, and Ar^* specie is approximately calculated out as 0.48 eV ion^{-1}, 0.05 eV atom^{-1}, 0.03 eV ion^{-1}, and 0.03 eV atom^{-1}, respectively. It is obvious that the incidence of Cr^+ ions is the most efficient energy transfer process.

Coating formation is known to occur *i* in three stages: *island nucleation and growth*, *island coalescence* and *continuous film growth*. The island density and the diffusion of adatoms on the growth surface are decisive for the microstructural evolution and resulting coating properties, such as roughness, grain size, and grain boundary, etc. The island number density N_{is} is primarily determined by the ion flux and diffusion of adatoms by the relation [54]

$$N_{is} = \frac{n}{\Omega^{1/3}}\left(\frac{J^i}{D^i}\right)^{1/3} \tag{13}$$

n is a dimensionless pre-factor with a maximum value of 0.25. D^i is the diffusivity of adatoms which depends on the growth temperature and the energy barrier [55] (E_D, 0.22 eV [56])

$$D^i = \frac{1}{4} l^2 \nu_0 \exp\left(-\frac{E_D - E_i}{k_B T}\right) \tag{14}$$

where l is the distance between two neighboring diffusion sites, ν_0 is the attempt frequency for a jump on a close-packed surface. It is evident that relatively small variations of T and E_D induce relatively large changes in N_{is}. The effect of a modulated deposition flux on the nucleation density depends on the relationship between the time domain of the modulation and the lifetime of adatom (τ_D) [54]

$$\tau_D \approx \frac{1}{N_{is} D^i} \tag{15}$$

The vapor flux can be estimated from the Cr atom density and the deposition rate. The deposition rate of Cr coatings at 650 V, 700 V, and 750 V was 6.82 Å s^{-1}, 6.07 Å s^{-1}, and 4.82 Å s^{-1}, respectively. The Cr atom density at the substrate vicinity was about 1.2×10^{17} m^3 during the pulse duration time [37]. The adatom lifetime with the variation of the transferred energy per incident species is presented in figure 11(a). The influence of the vapor flux on the adatom lifetime is shown in figure 11(b). Apparently, both the vapor flux and the transferred energy can change the adatom lifetime on the growth surface, which means that both factors have large effects on the regulation of the adatom lifetime. A reduced adatom lifetime means an increased diffusivity of the adatoms, and a high probability of finding a site with minimized surface energy. The red dashed lines in Red dash lines in figures 11(a) and (b) indicate the time period (2 ms) of HiPIMS-Cr discharges, which corresponding to the frequency of 500 Hz in this work. That is, the deposition flux will arrive onto the Cr coating growing surface with a modulation time of 2 ms. When the modulation time of deposition flux is shorter than the estimated adatom life, the diffusion of adatoms will be impeded by the attachment of species. It can be seen from figure 11 that adatoms gaining energy from the incidence of Cr^+ ions will have sufficient time to arrive at a minimized surface

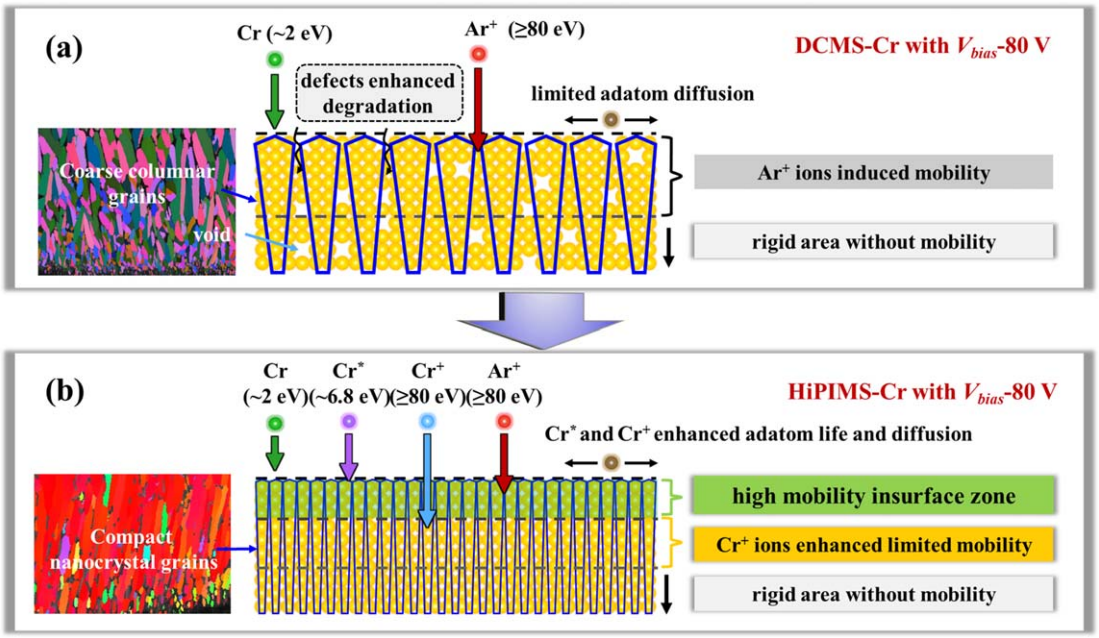

Figure 12. Schematic illustrations of Cr coating growth during (a) DCMS and (b) HiPIMS process with −80 V DC pulsed bias.

energy position in the modulation time of deposition flux. This explained why compact Cr coatings was deposited under an improved Cr^+ ions flux condition. As a result, a dense microstructure can be achieved when the adatoms gain more energy from the incident of energetic species.

Overall, during the HiPIMS deposition of Cr coatings with the pulse voltage of 650 V, the coating growing surface temperature increases with a value of ~100 K due to the high incident flux of Cr^* atoms. However, the Cr coating growth process is still in the transition zone according to the structural zone diagram proposed by A. Anders. Cr metal vapor flux with low fraction of ions could not be effectively energized by the substrate bias. Since only ions can gain kinetic energy from the electric field when passing through the plasma sheath. Therefore, when HiPIMS-Cr transfers into the low-density HiPIMS discharge mode at 750 V, the normalized energy flux is significantly improved. All the energetic species, including Cr^+ ions, Cr^* atoms, Ar^+ ions, and Ar^* atoms are able to enhance the diffusivity of Cr adatoms in the growing surface. However, the energy transfer caused by the incidence of Cr^+ ions is the most efficient process. HiPIMS-Cr discharge at 750 V with high metal ion fraction could effectively promote the diffusion of Cr adatoms. As a result, the compact Cr coating with a thickness of ~20 μm was prepared by the HiPIMS method with the pulse voltage of 750 V.

In the conventional DCMS processing, in addition to constant flux of low-energy Cr neutrals, the film growth surface is subjected to a large flux of gas ion irradiation (primarily Ar^+). As the Ar^+ energy ($\geqslant$80 eV) is larger than the lattice displacement threshold, such ion bombardment can induce continuous collision cascade events in the near-surface region (~1 nm), while the underlying structure is essentially frozen, leading to the formation of underdense microstructures with rough surfaces, as schematically illustrated in figure 12(a). However, the film growth pathway during the HiPIMS process is quite different, as shown in figure 12(b). While a high flux of Ar^+ ions, with an average energy $\geqslant$80 eV, is incident at the substrate during the HiPIMS pulses, Cr species, including neutral atoms with an average energy of ~2 eV, excited atoms with an average energy (counting additional potential energy) of ~6.8 eV and Cr^+ with average energy $\geqslant$ 80 eV, are also arrive and contribute to the total energy flux delivered to the substrate and thus modifying the microstructure of the advancing growth surface (both near-surface and sub-surface regions) during the 100 μs HiPIMS pulse, promoting the growth of dense and less defective Cr coatings [57].

5. Conclusions

HiPIMS has been successfully applied to deposit ultrathick (~20 μm) and compact Cr coating on Zry-4 alloys with a low deposition temperature of 200 °C. The nanocrystalline HiPIMS-Cr coating displays a smooth and compact microstructure without severe pores and penetrating defects, which appeared in the DCMS-Cr coating. When the discharge feature was changed from the 'low voltage DCMS-like' mode to the 'low density HiPIMS' mode, a rapid increase in the Cr^+ content at the substrate vicinity, which was determined from OES, was

obtained, indicating an enhanced energy flux to the deposited Cr coating. The generalized temperature increment of the growing surface Cr coating was ~100 K and was mainly affected by the incidence of Cr^* atoms. A simplified collision model was also proposed to calculate the energy transfer from the incident energetic species to the adatoms. The results show that the impingement of Cr^+ is the most efficient energy transfer process, which accounts for 0.48 eV ion^{-1} under the bias of −80 V in this work. The estimated adatom lifetime demonstrates that only those adatoms that gain energy from the incident Cr^+ ions can effectively diffuse and arrive at a minimized surface energy position on the growing surface within the modulation time of the deposition flux. This work reveals how discharge parameters control the microstructure of the Cr coating from the combined viewpoints of the HiPIMS-Cr deposition, the incidence of energetic species, and the diffusivity of Cr adatoms.

Acknowledgments

This work was supported by the National Natural Science Foundation of China (52025014, 52171090, 52101110), Zhejiang Provincial Natural Science Foundation of China (LQ22E010012), Ningbo Natural Science Foundation (2021J220). The authors would like to thank Mr Wentao Li for the SEM and EBSD measurements.

Data availability statement

All data that support the findings of this study are included within the article (and any supplementary files). Data will be available from 20 August 2023.

ORCID iDs

Guangxue Zhou https://orcid.org/0000-0001-8425-7820
Aiying Wang https://orcid.org/0000-0003-2938-5437

References

[1] Han X C, Chen C, Tan Y Q, Feng W L, Peng S M and Zhang H B 2020 A systematic study of the oxidation behavior of Cr coatings on Zry4 substrates in high temperature steam environment *Corros. Sci.* **174** 108826
[2] Tang C, Stüber M, Seifert H J and Steinbrück M 2020 Metallic and ceramic coatings for enhanced accident tolerant fuel cladding *Comprehensive Nuclear Materials* **4** 490–514
[3] Tang C C, Steinbrueck M, Stueber M, Grosse M, Yu X J, Ulrich S and Seifert H J 2018 Deposition, characterization and high-temperature steam oxidation behavior of single-phase Ti_2AlC-coated Zircaloy-4 *Corros. Sci.* **135** 87–98
[4] Zhong W C, Mouche P A, Han X C, Heuser B J, Mandapaka K K and Was G S 2016 Performance of iron-chromium-aluminum alloy surface coatings on Zircaloy 2 under high-temperature steam and normal BWR operating conditions *J. Nucl. Mater.* **470** 327–38
[5] Al-Olayyan Y, Fuchs G E, Baney R and Tulenko J 2005 The effect of Zircaloy-4 substrate surface condition on the adhesion strength and corrosion of SiC coatings *J. Nucl. Mater.* **346** 109–19
[6] Tang C C, Stueber M, Seifert H J and Steinbrueck M 2017 Protective coatings on zirconium-based alloys as accident-tolerant fuel (ATF) claddings *Corros. Rev.* **35** 141–65
[7] Yeom H, Maier B, Johnson G, Dabney T, Lenling M and Sridharan K 2019 High temperature oxidation and microstructural evolution of cold spray chromium coatings on Zircaloy-4 in steam environments *J. Nucl. Mater.* **526** 151737
[8] Maier B, Yeom H, Johnson G, Dabney T, Walters J, Xu P, Romero J, Shah H and Sridharan K 2019 Development of cold spray chromium coatings for improved accident tolerant zirconium-alloy cladding *J. Nucl. Mater.* **519** 247–54
[9] Kim H G, Kim I H, Jung Y I, Park D J, Park J Y and Koo Y H 2015 Adhesion property and high-temperature oxidation behavior of Cr-coated Zircaloy-4 cladding tube prepared by 3D laser coating *J. Nucl. Mater.* **465** 531–9
[10] Kashkarov E B, Sidelev D V, Rombaeva M, Syrtanov M S and Bleykher G A 2020 Chromium coatings deposited by cooled and hot target magnetron sputtering for accident tolerant nuclear fuel claddings *Surf. Coat. Technol.* **389** 125618
[11] Wei T G, Zhang R Q, Yang H Y, Liu H, Qiu S Y, Wang Y, Du P N, He K, Hu X G and Dong C 2019 Microstructure, corrosion resistance and oxidation behavior of Cr-coatings on Zircaloy-4 prepared by vacuum arc plasma deposition *Corros. Sci.* **158** 108077
[12] Hu X G, Dong C, Wang Q, Chen B Q, Yang H Y, Wei T G, Zhang R Q, Gu W and Chen D M 2019 High-temperature oxidation of thick Cr coating prepared by arc deposition for accident tolerant fuel claddings *J. Nucl. Mater.* **519** 145–56
[13] Han X C, Xue J X, Peng S M and Zhang H B 2019 An interesting oxidation phenomenon of Cr coatings on Zry-4 substrates in high temperature steam environment *Corros. Sci.* **156** 117–24
[14] Park J H, Kim H G, Park J Y, Jung Y I, Park D J and Koo Y H 2015 High temperature steam-oxidation behavior of arc ion plated Cr coatings for accident tolerant fuel claddings *Surf. Coat. Technol.* **280** 256–9
[15] Brachet J C *et al* 2020 High temperature steam oxidation of chromium-coated zirconium-based alloys: Kinetics and process *Corros. Sci.* **167** 108537
[16] Brachet J C *et al* 2019 Early studies on Cr-Coated Zircaloy-4 as enhanced accident tolerant nuclear fuel claddings for light water reactors *J. Nucl. Mater.* **517** 268–85
[17] Bischoff J *et al* 2018 AREVA NP's enhanced accident-tolerant fuel developments: Focus on Cr-coated M5 cladding *Nuclear Engineering and Technology* **50** 223–8

[18] Yang J, Steinbrück M, Tang C, Große M, Liu J, Zhang J, Yun D and Wang S 2022 Review on chromium coated zirconium alloy accident tolerant fuel cladding *J. Alloy. Compd.* **895** 162450
[19] Ma H B, Yan J, Zhao Y H, Liu T, Ren Q S, Liao Y H, Zuo J D, Liu G and Yao M Y 2021 Oxidation behavior of Cr-coated zirconium alloy cladding in high-temperature steam above 1200 °C *npj Mat. Degrad.* **5** 1–11
[20] Shaginyan L, Han J G and Lee H M 2004 Structural nomuniformity and internal stress in chromium films deposited by magnetron sputtering *Jpn. J. Appl. Phys.* **43** 2594–601
[21] Janssen G C A M, Alkemade P F A, Sivel V G M, Grachev S Y and Kamminga J D 2004 Anisotropic growth of chromium films during sputter deposition on substrates in planetary motion *J. Vac. Sci. Technol. A* **22** 1773–7
[22] Lintymer J, Gavoille J, Martin N and Takadoum J 2003 Glancing angle deposition to modify microstructure and properties of sputter deposited chromium thin films *Surf. Coat. Technol.* **174** 316–23
[23] Patten J W and Mcclanahan E D 1972 Effect of substrate bias and deposition temperature on properties of thick sputtered chromium deposits *J. Appl. Phys.* **43** 4811–3
[24] Xin C, Yang D, Sun Q, Xiao L and Sun J 2019 Thermal stability of nanogradient microstructure produced by surface mechanical rolling treatment in Zircaloy-4 *J. Mater. Sci.* **55** 4926–39
[25] Hiwarkar V D, Sahoo S K, Samajdar I, Satpathy A, Krishna K V M, Dey G K, Srivastav D, Tewari R and Banarjee S 2011 Defining recrystallization in pilgered Zircaloy-4: From preferred nucleation to growth inhibition *J. Nucl. Mater.* **412** 287–93
[26] Dunlop J W C, Brechet Y J M, Legras L and Zurob H S 2007 Modelling isothermal and non-isothermal recrystallisation kinetics: Application to Zircaloy-4 *J. Nucl. Mater.* **366** 178–86
[27] Zhu Y and Zhang X 2009 Effect of surface nanocrystallization on the corrosion behavior of Zircaloy-4 *Sci. China Ser. E.* **52** 2227–31
[28] Zhang X Y, Shi M H, Li C, Liu N F and Wei Y M 2007 The influence of grain size on the corrosion resistance of nanocrystalline zirconium metal *Mat. Sci. Eng. A-Struct* **448** 259–63
[29] Anders A 2010 A structure zone diagram including plasma-based deposition and ion etching *Thin Solid Films* **518** 4087–90
[30] Stringer J 1987 Role of Coatings in Energy-Producing Systems - an Overview *Mater. Sci. Eng.* **87** 1–10
[31] Anders A 2014 A review comparing cathodic arcs and high power impulse magnetron sputtering (HiPIMS) *Surf. Coat. Technol.* **257** 308–25
[32] Alami J, Maric Z, Busch H, Klein F, Grabowy U and Kopnarski M 2014 Enhanced ionization sputtering: A concept for superior industrial coatings *Surf. Coat. Technol.* **255** 43–51
[33] Sarakinos K, Alami J and Konstantinidis S 2010 High power pulsed magnetron sputtering: A review on scientific and engineering state of the art *Surf. Coat. Technol.* **204** 1661–84
[34] Rudolph M, Brenning N, Raadu M A, Hajihoseini H, Gudmundsson J T, Anders A and Lundin D 2020 Optimizing the deposition rate and ionized flux fraction by tuning the pulse length in high power impulse magnetron sputtering *Plasma Sources Sci. T.* **29** 05LT01
[35] Anders A 2017 Tutorial: Reactive high power impulse magnetron sputtering (R-HiPIMS) *J. Appl. Phys.* **121** 171101
[36] Zuo X, Ke P L, Chen R D, Li X W, Oden M and Wang A Y 2017 Discharge state transition and cathode fall thickness evolution during chromium HiPIMS discharge *Phys. Plasmas* **24** 083507
[37] Zuo X, Zhang D, Chen R D, Ke P L, Oden M and Wang A Y 2020 Spectroscopic investigation on the near-substrate plasma characteristics of chromium HiPIMS in low density discharge mode *Plasma Sources Sci. T.* **29** 015013
[38] Anders A 2010 Deposition rates of high power impulse magnetron sputtering: Physics and economics *J. Vac. Sci. Technol. A* **28** 783–90
[39] Yushkov G Y and Anders A 2010 Origin of the Delayed Current Onset in High-Power Impulse Magnetron Sputtering *IEEE Trans. Plasma Sci.* **38** 3028–34
[40] Aiempanakit M, Aijaz A, Lundin D, Helmersson U and Kubart T 2013 Understanding the discharge current behavior in reactive high power impulse magnetron sputtering of oxides *J. Appl. Phys.* **113** 133302
[41] Huang M J, Li Y P, Ran G, Yang Z B and Wang P H 2020 Cr-coated Zr-4 alloy prepared by electroplating and its *in situ* He+ irradiation behavior *J. Nucl. Mater.* **538** 152240
[42] Sarakinos K, Magnfalt D, Elofsson V and Lu B 2014 Atomistic view on thin film nucleation and growth by using highly ionized and pulsed vapour fluxes *Surf. Coat. Technol.* **257** 326–32
[43] Rudolph M, Lundin D, Foy E, Debongnie M, Hugon M C and Minea T 2018 Influence of backscattered neutrals on the grain size of magnetron-sputtered TaN thin films *Thin Solid Films* **658** 46–53
[44] Zambrano G, Riascos H, Prieto P, Restrepo E, Devia A and Rincon C 2003 Optical emission spectroscopy study of r.f. magnetron sputtering discharge used for multilayers thin film deposition *Surf. Coat. Technol.* **172** 144–9
[45] West G, Kelly P, Barker P, Mishra A and Bradley J 2009 Measurements of deposition rate and substrate heating in a hipims discharge *Plasma Processes Polym.* **6** S543–7
[46] Lundin D, Stahl M, Kersten H and Helmersson U 2009 Energy flux measurements in high power impulse magnetron sputtering *J. Phys. D: Appl. Phys.* **42** 185202
[47] Nafarizal N and Sasaki K 2007 Sticking probability of Ti atoms in magnetron sputtering deposition evaluated from the spatial distribution of Ti atom density *J. Vac. Sci. Technol. A* **25** 308–11
[48] Wilson R J and Mills A P 1983 Electron and positron work functions of Cr (100) *Surf. Sci.* **128** 70–80
[49] Kaoumi D, Motta A T and Birtcher R C 2008 A thermal spike model of grain growth under irradiation *J. Appl. Phys.* **104** 073525
[50] Wu H C and Anders A 2010 Energetic deposition of metal ions: observation of self-sputtering and limited sticking for off-normal angles of incidence *J. Phys. D: Appl. Phys.* **43** 065206
[51] Lee W W Y and Oblas D 1975 Argon entrapment in metal films by dc triode sputtering *J. Appl. Phys.* **46** 1728–32
[52] Filinov A V, Michael B and Detlef L 2018 Microscopic modeling of gas-surface scattering. I. A combined molecular dynamics-rate equation approach *Plasma Sources Sci. T.* **27** 064003
[53] Zhou X W and Wadley H N G 2001 The low energy ion assisted control of interfacial structure: ion incident angle effects *Surf. Sci.* **487** 159–70
[54] Magnfalt D, Elofsson V, Abadias G, Helmersson U and Sarakinos K 2013 Time-domain and energetic bombardment effects on the nucleation and coalescence of thin metal films on amorphous substrates *J. Phys. D: Appl. Phys.* **46** 215303
[55] Makeev M A and Barabasi A L 1997 Ion-induced effective surface diffusion in ion sputtering *Appl. Phys. Lett.* **71** 2800–2
[56] Sligte E T, van der Stam K M R, Smeets B, van der Straten P, Scholten R E, Beijerinck H C W and van Leeuwen K A H 2004 Barrier-limited surface diffusion in atom lithography *J. Appl. Phys.* **95** 1749–55
[57] Farhadizadeh A and Kozak T 2022 The importance of discharge voltage in DC magnetron sputtering for energy of sputtered and backscattered atoms on the substrate: Monte-Carlo simulations *Vacuum* **196** 110716